The Astrophysical Journal, 1002:102 (12pp), 2026 May 1 https://doi.org/10.3847/1538-4357/ae5c9d

The Long Quest for Vacuum Birefringence in Magnetars: 1E 1547.0–5408 and the Elusive Smoking Gun

Roberto Taverna[1], Roberto Turolla[1,2], Lorenzo Marra[3], Ruth M.E. Kelly[2], Alice Borghese[4], Gian Luca Israel[5], Sandro Mereghetti[6], Andrea Possenti[7], Silvia Zane[2], and Michela Rigoselli[6,8]
[1] Department of Physics and Astronomy, University of Padova, via Marzolo 8, I-35131 Padova, Italy
[2] Mullard Space Science Laboratory, University College London, Holmbury St Mary, Dorking, Surrey RH5 6NT, UK
[3] INAF—Istituto di Astrofisica e Planetologia Spaziali, Via del Fosso del Cavaliere 100, I-00133, Roma, Italy
[4] European Space Agency (ESA), European Space Astronomy Centre (ESAC), Camino Bajo del Castillo s/n, 28692, Villanueva de la Cañada, Madrid, Spain
[5] INAF—Osservatorio Astronomico di Roma, via Frascati 33, I-00078 Monteporzio Catone, Italy
[6] INAF—Istituto di Astrofisica Spaziale e Fisica Cosmica di Milano, via Corti 12, I-20133 Milano, Italy
[7] INAF—Osservatorio Astronomico di Cagliari, via della Scienza 5, I-00947 Selargius, Italy
[8] INAF—Osservatorio Astronomico di Brera, via Brera 28, I-20121 Milano, Italy
Received 2026 January 21; revised 2026 April 6; accepted 2026 April 6; published 2026 April 28

Abstract

Magnetars are now known to be among the most strongly polarized celestial sources in X-rays. Here, we report on the 500 ks observation of the magnetar 1E 1547.0−5408 performed by the Imaging X-ray Polarimetry Explorer (IXPE) in 2025 March. The IXPE spectrum is well reproduced by a single thermal component with blackbody temperature $kT_{\rm BB} \sim 0.67$ keV and emission radius $R_{\rm BB} \sim 1.2$ km. The source exhibits a high linear polarization degree in the 2–6 keV band (PD = 47.7% ± 2.9%) with polarization angle PA = 75.°8 ± 1.°8, measured west of celestial north. While PA does not appear to vary with energy, there is some evidence (at the 1σ confidence level) of a minimum in PD between 3 and 4 keV, compatible with what is expected by partial mode conversion at the vacuum resonance in a magnetized atmosphere. Phase-resolved spectral and polarimetric analyses reveal that X-ray thermal radiation likely originates from a single, fairly small hot spot with a nonuniform temperature distribution. Fitting the phase-dependent PA measured by IXPE with a rotating vector model (RVM) constrains the source geometry and indicates that both the dipole axis and line-of-sight are misaligned with respect to the spin axis. Under these conditions, the high polarization of the source cannot be regarded as compelling evidence for the presence of vacuum birefringence in the star's magnetosphere. Nevertheless, the fact that the RVM successfully reproduces the modulation of the X-ray polarization angle and the behavior of PD with the energy hint once more at the presence of QED effects in magnetars.

Unified Astronomy Thesaurus concepts: Magnetars (992); Neutron stars (1108); Polarimetry (1278); Single x-ray stars (1461)

1. Introduction

Soft gamma repeaters (SGRs) and anomalous X-ray pulsars (AXPs) form a distinct class of Galactic X-ray pulsars characterized by long rotational periods, $P \approx 1$–12 s, and large spin-down rates, $\dot{P} \approx 10^{-15}$–10^{-10} s s^{-1}. These sources produce recurrent, subsecond bursts of hard X-ray/soft-γ radiation and exhibit persistent X-ray luminosities of $L_{\rm X} \approx 10^{30}$–$10^{35}$ erg s^{-1}, typically exceeding their rotational energy losses. Their timing properties imply surface dipole magnetic fields of $B \approx 10^{13}$–10^{15} G, and the absence of detectable companions identifies them as magnetars: neutron stars powered primarily by the decay and dissipation of ultrastrong magnetic fields (R. C. Duncan & C. Thompson 1992; C. Thompson & R. C. Duncan 1993, see also R. Turolla et al. 2015; V. M. Kaspi & A. M. Beloborodov 2017 for reviews).

Below ∼10 keV, magnetar spectra are commonly represented by two-component models, either two blackbodies (BBs) or a BB plus a power law (PL). The thermal components arise from localized hot spots on the neutron star's surface, whereas the nonthermal component is produced via resonant Compton scattering (RCS) of surface photons by magnetospheric charges in a twisted magnetic field (C. Thompson et al. 2002; R. Fernández & C. Thompson 2007; L. Nobili et al. 2008). Many magnetars also emit a hard X-ray tail extending up to ∼100–200 keV, often with strong pulsations.

In such extreme magnetic environments, the propagation of electromagnetic radiation is profoundly modified, as first discussed in the pioneering work of Y. N. Gnedin et al. (1978a, 1978b, see also J. S. Heyl & L. Hernquist 1997 and A. K. Harding & D. Lai 2006 for a comprehensive review). The combined plasma–vacuum dielectric tensor becomes highly anisotropic, and the ordinary (O) and extraordinary (X) polarization eigenmodes acquire markedly different opacities. Radiative-transfer calculations predict correspondingly large linear polarization fractions, up to ∼80% and ∼20%, from thermal emission emerging from strongly magnetized atmospheres or condensed surfaces, respectively (e.g., R. Fernández & S. W. Davis 2011; R. Taverna et al. 2014, 2020). Until recently, these predictions remained untested, owing to the lack of sensitivity in X-ray polarimeters.

The launch of the Imaging X-ray Polarimetry Explorer (IXPE) in 2021 December (M. C. Weisskopf et al. 2022) enabled the first high-quality spectropolarimetric measurements in the 2–8 keV band. During its four years of operations,

IXPE observed about one hundred X-ray sources, including five persistent magnetars, 4U 0142+61 (R. Taverna et al. 2022), 1RXS J170849.0−400910 (hereafter 1RXS J1708; S. Zane et al. 2023), SGR 1806−20 (R. Turolla et al. 2023), 1E 2259+586 (J. Heyl et al. 2024), and 1E 1841−045 (M. Rigoselli et al. 2025; R. E. Stewart et al. 2025a). With the exception of SGR 1806−20, statistically significant polarization (energy and phase integrated) was detected, ranging from ≈6% to ≈35%. The degree of polarization is strongly dependent on the energy: it is moderate (≈10%–20%) at 2–3 keV and then increases to ≈60%–80% at 6–8 keV in 1E 1841−045 and 1RXS J1708, or to ≈35% in 4U 0142+61. The polarization angle remains nearly constant with the energy in the former two sources, implying that the same polarization mode dominates through the IXPE band. In contrast, 4U 0142+61 exhibits a drop in the polarization degree to zero near 4 keV accompanied by ∼90° rotation of the polarization angle, signaling a transition in the prevailing polarization mode (see R. Taverna & R. Turolla 2024, for an extensive discussion and D. Lai 2023 for an alternative interpretation).

In this paper, we report on the spectral and polarization analysis of the IXPE observation of the magnetar 1E 1547.0−5408, targeted in the GO2 observing run (P.I. George Younes). We provide a comparative assessment of our findings against those recently presented in a preprint by R. E. Stewart et al. (2025b) and highlight similarities and differences between their (preliminary) analysis and the present one. Observations and data processing are detailed in Section 2. The results of our spectral, timing, and polarimetric analyses are presented in Section 3 and discussed in Section 4. Conclusions follow in Section 5.

2. Observations and Data Analysis

The IXPE observation of 1E 1547.0−5408 started on 2025 March 26 03:01:52 UTC and ended on 2025 April 5 00:26:53 UTC, for a total on-source exposure time of ≈500 ks. After retrieving the level 1 and level 2 data files from the HEASARC IXPE public archive,[9] we referred the event arrival times to the solar system barycenter using the ftool `barycorr` with JPL planetary ephemerids DE430 (R.A. $= 15^{\rm h}\,50^{\rm m}\,54\overset{\rm s}{.}12386$, DEC $= -54^{\circ}\,18'\,24\overset{''}{.}1131$, taken from the ATNF Pulsar Catalog,[10] R. N. Manchester et al. 2005), and performed proper background rejection, according to the procedure discussed in A. Di Marco et al. (2023); furthermore, some time intervals containing the most prominent background spikes, for a total of $\lesssim$100 s, were removed from the dataset. We then extracted from the resulting photon lists the source counts from a circle of radius $r^{\rm src}$, centered on the position of the source and subtracted the background counts taken from a concentric annular region, with inner and outer radii $r_{\rm inn}^{\rm bkg}$ and $r_{\rm out}^{\rm bkg}$, respectively. Following the procedure outlined in E. Piconcelli et al. (2004), we find that the best signal-to-noise ratio is obtained for $r^{\rm src} = 60''$, $r_{\rm inn}^{\rm bkg} = 120''$ and $r_{\rm out}^{\rm bkg} = 240''$; this produced about 25, 600 source counts summed over the three IXPE detector units (DUs). By taking $r^{\rm src} \lesssim 50''$, an increasing fraction of the source photons is lost, up to ∼20% when $r^{\rm src}$ shrinks to ∼30″.

The source counts are completely dominated by the background above ≈6 keV, preventing a meaningful spectropolarimetric analysis at higher energies (see Section 3.2). We therefore opted to restrict our investigation to the 2–6 keV energy band and to use the weighted analysis procedure. To this end, we processed the level 2 files using the latest version of the IXPE response functions (20250225), available online in the HEASARC calibration database.[11]

3. Results

3.1. Timing Analysis

We processed the level 2 photon lists using version 8.1 of the HENDRICS package (M. Bachetti 2018, see also M. Bachetti et al. 2015 for a complete description of the STINGRAY software) to compute the timing solution for 1E 1547.0−5408. The most prominent peak in the frequency spectrum appears in the 0.45–0.50 Hz interval, within which we then performed a Z_n^2 search. Sinusoidal pulsations were detected at a frequency $\nu_0 = 0.47785498(2)$ Hz, with a frequency derivative $\dot{\nu}_0 = -4.7(6) \times 10^{-12}$ Hz s^{-1}. The times-of-arrival (TOAs) of the events were then calculated using the `HENphaseogram` tool, dividing the observation into 75 time intervals. Finally, by fitting the TOAs with a linear spin-down relation $\nu = \nu_0 + \dot{\nu}_0 t$ with the PINT software (v1.1.4, J. Luo et al. 2021), we obtained the best-fitting spin frequency and frequency derivative as $\nu = 0.477855133 \pm 2.1 \times 10^{-8}$ Hz and $\dot{\nu} = -(4.68 \pm 0.19) \times 10^{-12}$ Hz/s (χ^2/dof $= 40.832/76$), respectively, at epoch 60765.0724 MJD; the corresponding values of the period and period derivative are $P = 2.092684438 \pm 9.4 \times 10^{-8}$ s and $\dot{P} = (2.05 \pm 0.08) \times 10^{-11}$ s/s [12] (for a spin-down dipole magnetic field strength $B_{\rm sd} \approx 2 \times 10^{14}$ G at the magnetic equator). This timing solution was then used to phase-fold the photon lists with the `xpphase` tool within the IXPEOBSSIM package (L. Baldini et al. 2022, see Section 3.5).

3.2. Phase-averaged Spectral Analysis

We processed data from the three IXPE DUs within XSPEC (K. A. Arnaud 1996), generating the ancillary response files (ARFs) and modulation response files (MRFs) with the IXPECALCARF tool (C.-T. Chen & IXPE Science Operation Center 2025). Data were grouped to ensure a signal-to-noise ratio $\gtrsim$3 in each bin in the 2–6 keV energy band. A normalization factor was included in all the models to account for the different cross-calibrations of the three DUs (assuming unity for DU1). Interstellar absorption was modeled using `tbabs`, with abundances taken from J. Wilms et al. (2000) and photoionization cross-sections from D. A. Verner et al. (1996). We adopted the column density $N_{\rm H} = 4.6 \times 10^{22}$ cm^{-2} quoted in the systematic study by F. Coti Zelati et al. (2020), based on XMM-Newton, Chandra, and Swift-XRT data collected between 2009 and 2017 (see F. Coti Zelati et al. 2018), since the limited coverage of IXPE at low energies does not allow a precise determination of $N_{\rm H}$. We first attempted a fit using a single absorbed BB component (`tbabs×bbody-rad`). The model shows a good agreement with the data (see Figure 1 and Table 1), with χ^2/dof $= 263.95/248$. The resulting BB temperature, ≈0.67 keV, is fully consistent with the values reported from observations taken shortly after the

[9] https://heasarc.gsfc.nasa.gov/docs/ixpe/archive
[10] https://www.atnf.csiro.au/research/pulsar/psrcat
[11] https://heasarc.gsfc.nasa.gov/docs/ixpe/caldb
[12] Here and in the following, errors are quoted at 1σ confidence level, unless explicitly stated otherwise.

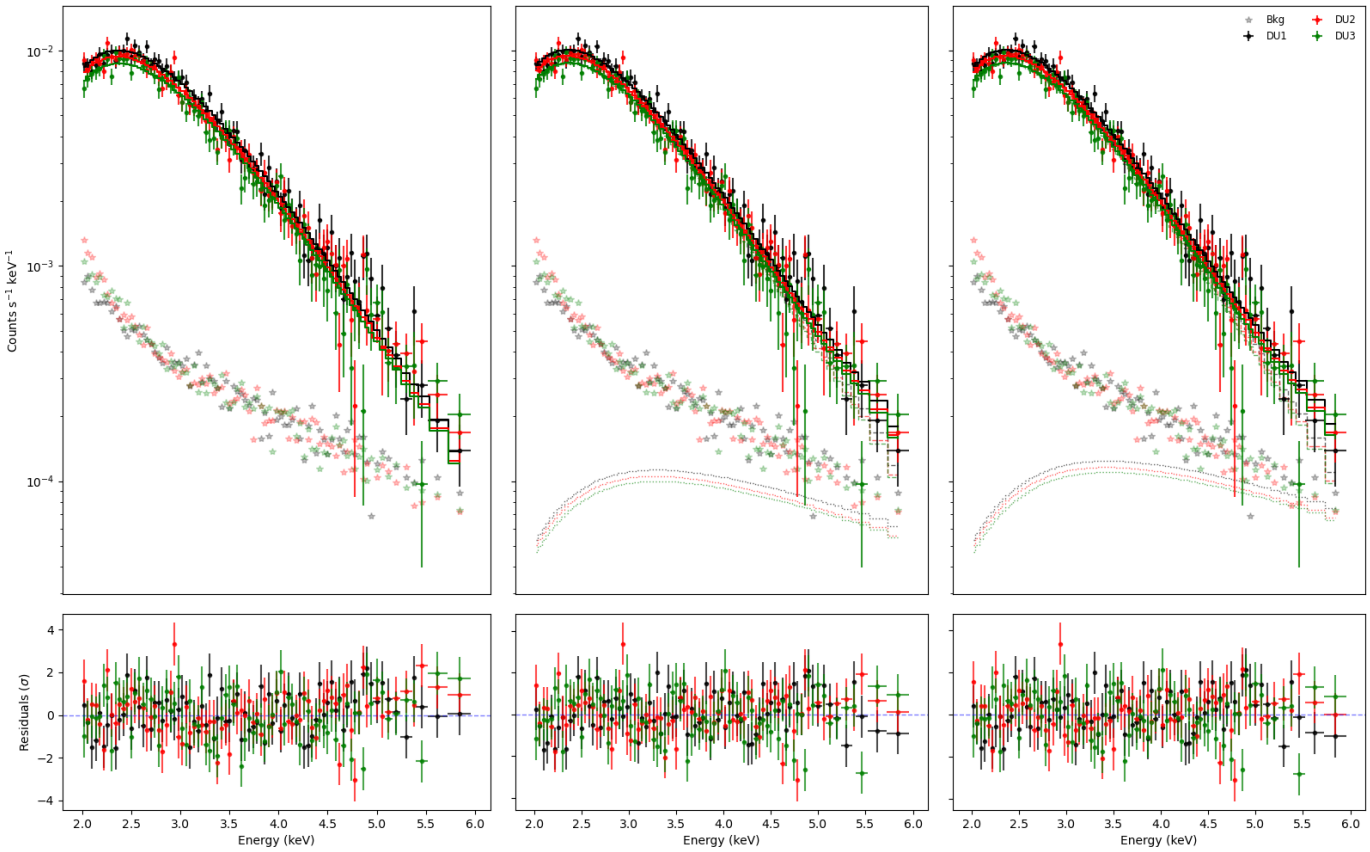

Figure 1. IXPE source (dots with error bars) and background (stars) spectra (top panel) of 1E 1547.0−5408 collected by DU1 (black), DU2 (red), and DU3 (green), and fitting residuals in units of the standard deviation (bottom panels) for the `tbabs×bbodyrad` model with $N_{\rm H}$ frozen at $4.6 \times 10^{22}\,{\rm cm}^{-2}$ (left), `tbabs×(bbodyrad+bbodyrad)` model with $N_{\rm H}$ frozen at $4.6 \times 10^{22}\,{\rm cm}^{-2}$ (center) and `tbabs×(bbodyrad+powerlaw)` model with $N_{\rm H}$ frozen at $4.9 \times 10^{22}\,{\rm cm}^{-2}$ (right). The best-fitting models (solid histograms) and the individual components (dotted histograms) are also shown in each plot. Fit results are summarized in Table 1.

2009 outburst of 1E 1547.0−5408 (see F. Bernardini et al. 2011). However, the corresponding emission radius, ≈1.2 km for a distance of 4.5 kpc (A. Tiengo et al. 2010), is somewhat smaller and more in line with the most recent estimates (F. Coti Zelati et al. 2020; M. E. Lower et al. 2023). This discrepancy is most likely due to the larger size of the emitting region during an outburst phase, which then shrinks as the source returns in quiescence (see e.g., D. De Grandis et al. 2022).

For completeness, and given that previous studies of the source at soft X-ray energies showed the presence of a second spectral component (F. Bernardini et al. 2011; F. Coti Zelati et al. 2020), we also considered adding either a BB or a PL to the model. Keeping $N_{\rm H}$ fixed at the above value, the fit with two BBs, `tbabs×(bbodyrad+bbodyrad)`, is also good, with $\chi^2/{\rm dof} = 255.50/242$. The spectral parameters of the softer component are well constrained and similar to those obtained previously ($kT_1 = 0.65$ keV, $R_{\rm BB_1} = 1.3$ km), while those of the hotter one are totally unconstrained. Similar results were obtained with a BB plus PL model, `tbabs×(bbodyrad+powerlaw)`, fixing $N_{\rm H}$ to the value obtained by F. Coti Zelati et al. (2018) using a BB+2PL decomposition ($4.9 \times 10^{22}\,{\rm cm}^{-2}$). The fit is also statistically satisfactory ($\chi^2/{\rm dof} = 253.94/242$), with BB temperature (0.64 keV) and radius (1.4 km) compatible with those obtained before, but the nonthermal component remains completely unconstrained (see again Table 1 and Figure 1 for details).

We finally note that previous broad-band investigations of 1E 1547.0−5408 required the presence of an additional PL component at hard X-ray energies, dominating the spectrum above ≈10 keV (F. Bernardini et al. 2011; F. Coti Zelati et al. 2020; M. E. Lower et al. 2023). We do not include this component in our fits because its contribution in the IXPE energy range is negligible. For all these reasons, we adopted the single-BB model in the remainder of our spectropolarimetric analysis. Although our conclusions about the spectral model agree with those of R. E. Stewart et al. (2025b), the values of $kT_{\rm BB}$ and $R_{\rm BB}$ are not compatible within 3σ, possibly due to the different values assumed for $N_{\rm H}$.

3.3. Phase-resolved Spectral Analysis

Using the IXPEOBSSIM`xpphase` and `xpselect` tools, the data were folded into seven equally spaced phase bins, based on the timing solution presented in Section 3.1. We then extracted the source and background spectra in each phase bin, and, according to the results of the phase-averaged analysis discussed in Section 3.2, we fit the data using a single-component model (`tbabs×bbodyrad`), with the column density $N_{\rm H}$ frozen to the value reported in Table 1.[13]

Table 2 reports the best-fitting parameters for each phase bin, together with the corresponding unabsorbed and observed

[13] We verified that, similarly to what was found in the phase-averaged spectral analysis, a second spectral component is not statistically required.

Table 1
Phase-averaged Spectral Analysis of the IXPE Data

	tbabs×bbodyrad	tbabs×(bbodyrad+bbodyrad)	tbabs×(bbodyrad+powerlaw)
$N_{\rm H}$ (10^{22} cm^{-2})	4.6[a]	4.6[a]	4.9[a]
kT_1 (keV)	$0.674^{+0.006}_{-0.005}$	$0.653^{+0.009}_{-0.009}$	$0.638^{+0.011}_{-0.018}$
$R_{\rm BB_1}$[b] (km)	$1.20^{+0.02}_{-0.02}$	$1.27^{+0.04}_{-0.03}$	$1.36^{+0.06}_{-0.05}$
kT_2 (keV)	⋯	< 200	⋯
$R_{\rm BB_2}$[b] (km)	⋯	$1.91^{+182.86}_{-0.20} \times 10^{-3}$	⋯
$\Gamma_{\rm PL}$	⋯	⋯	$-1.14^{+2.81}_{-1.10}$
norm$_{\rm PL}$[c]	⋯	⋯	$3.46^{+571.08}_{-3.21} \times 10^{-6}$
$F^{2-6}_{\rm unabs}$[d]	$9.29^{+0.07}_{-0.07}$	$9.37^{+0.07}_{-0.07}$	$9.69^{+0.07}_{-0.07}$
$F^{2-6}_{\rm obs}$[e]	$5.81^{+0.04}_{-0.04}$	$5.87^{+0.04}_{-0.04}$	$5.87^{+0.04}_{-0.04}$
const$_{\rm DU_1}$	1.00[a]	1.00[a]	1.00[a]
const$_{\rm DU_2}$	$1.02^{+0.02}_{-0.02}$	$1.03^{+0.02}_{-0.02}$	$1.02^{+0.02}_{-0.02}$
const$_{\rm DU_3}$	$0.95^{+0.02}_{-0.02}$	$0.95^{+0.02}_{-0.02}$	$0.95^{+0.02}_{-0.02}$
χ^2/dof	263.95/244	255.50/242	253.94/242

Notes.
[a] Frozen parameters.
[b] Emission radius extracted from the bbodyrad parameter norm assuming a distance of 4.5 kpc (A. Tiengo et al. 2010).
[c] Normalization of the powerlaw component in photons keV^{-1} cm^{-2} s^{-1} at 1 keV.
[d] Total unabsorbed 2–6 keV flux in units of 10^{-12} erg cm^{-2} s^{-1}.
[e] Total observed 2–6 keV flux in units of 10^{-12} erg cm^{-2} s^{-1}.

fluxes. The χ^2/dof values indicate that the model provides an acceptable fit at a confidence level greater than 99% in all phase bins. The pulse profile in the 2–6 keV energy range is shown in Figure 2, along with those in the 2–3, 3–4, 4–5, and 5–6 keV energy bins. The average values of the unabsorbed and observed fluxes, $(9.14 \pm 0.07) \times 10^{-12}$ erg cm^{-2} s^{-1} and $(5.70 \pm 0.04) \times 10^{-12}$ erg cm^{-2} s^{-1}, respectively, are consistent with the corresponding phase-averaged values (see Table 1) at 2σ confidence level. The measured pulsed fraction (PF, see Table 3) increases monotonically with energy from $31.9\% \pm 1.3\%$ at 2–3 keV to $56.5\% \pm 1.0\%$ at 5–6 keV (the constant-PF hypothesis is rejected at more than 10σ). The averaged PF in the 2–6 keV is $38.1\% \pm 1.3\%$.

Figure 3 shows the phase dependence of the temperature and emission radius for the best-fitting spectral model. While $R_{\rm BB}$ is consistent with a constant value (1.22 ± 0.07 km) at the 1σ confidence level, in agreement with the emission radius inferred from the phase-averaged spectrum (see Table 1), the BB temperature shows a clear oscillation in phase with the pulse profile (see Figure 2).

3.4. Phase-averaged Polarimetric Analysis

We processed the source photon lists using the same procedure described in Section 3.2 and Section 3.3 to extract the Q and U Stokes parameters as functions of photon energy and rotational phase. We followed the method discussed in T. E. Strohmayer (2017), simultaneously fitting the I, Q, and U spectra in different energy intervals within XSPEC, with the appropriate response functions; the Q and U data were grouped in such a way to ensure at least five counts per energy bin. We convolved a constant polarization model (polconst) to the tbabs×bbodyrad model (see Section 3.2) and froze the spectral parameters to the values obtained in the phase-averaged spectral fit (see Table 1). We note that this method is essentially independent of the specific spectral model adopted, provided that the energy intervals in which the polarization properties are extracted are sufficiently narrow. We checked a posteriori that the PD and PA values derived using the alternative spectral models reported in Table 1 differ only marginally from those obtained using the single-BB model, with deviations well within the 1σ confidence intervals.

The results for the phase-averaged degree and angle of polarization, integrated in the entire range 2–6 keV are shown in Figure 4 for each of the three DUs, together with the value obtained by combining the data from all DUs. The polarization degree for the combined DUs, PD $= \sqrt{(Q/I)^2 + (U/I)^2}$, is $47.7\% \pm 2.9\%$ and is significant at the level $\approx 16\sigma$. The associated polarization angle, PA $= \arctan(U/Q)/2$ is $75\overset{\circ}{.}8 \pm 1\overset{\circ}{.}8$, measured west of north. The values of PD and PA measured by the individual DUs differ by less than 1σ, and are entirely consistent with each other. All measurements are above MDP$_{99}$,[14] as certified by the fact that the 99% confidence contours in the PD–PA polar plane are closed.

The energy-dependent degree and angle of polarization in the range 2–6 keV are shown in Figure 5, while the best-fit values obtained in the different energy intervals are reported in Table 3 (along with the corresponding PF). When the most-probable value of PD in a given energy interval falls below the corresponding MDP$_{99}$ (i.e., when the corresponding 99% confidence contour remains open in the bottom panel of Figure 5), the 3σ upper limit is reported in the top panel of Figure 5, while PA is unconstrained and marked by a double arrow. Significant polarization is detected only at energies below 5 keV, which is in agreement with the discussion in Section 2. In bins where the polarization measure is significant, the PD appears to vary with energy, showing a minimum between 3 and 4 keV. Taking into account also the most-probable value of PD in the bin 5–6 keV, the hypothesis of a constant PD is marginally rejected at the confidence level of 94.9% (χ^2/dof $= 7.75/3$, for a fit to a constant PD). Considering, instead, only the three energy bins where the polarization degree is significant, the constant fit is ruled out at 97.6% confidence level (χ^2/dof $= 7.48/2$). This is supported by the confidence contours shown in Figure 5: the 68% contours of the 3–4 keV and the

[14] The minimum detectable polarization at the 99% confidence level as defined in M. C. Weisskopf et al. (2010).

Table 2
Phase-resolved Spectral Fit of the IXPE Data in the 2–6 keV Band

Spectral model: tbabs×bbodyrad[a]					
Phase Bin	kT (keV)	R_{BB} (km)[b]	F_{unabs}[c]	F_{obs}[d]	χ^2/dof
0.00–0.14	$0.610^{+0.018}_{-0.017}$	$1.24^{+0.24}_{-0.23}$	$6.05^{+0.15}_{-0.15}$	$3.63^{+0.09}_{-0.09}$	127.00/131
0.14–0.29	$0.641^{+0.018}_{-0.017}$	$1.11^{+0.21}_{-0.20}$	$6.27^{+0.15}_{-0.15}$	$3.84^{+0.09}_{-0.09}$	103.07/128
0.29–0.43	$0.667^{+0.017}_{-0.017}$	$1.17^{+0.21}_{-0.19}$	$8.46^{+0.17}_{-0.17}$	$5.26^{+0.11}_{-0.11}$	128.68/149
0.43–0.57	$0.691^{+0.014}_{-0.014}$	$1.25^{+0.20}_{-0.19}$	$11.49^{+0.20}_{-0.20}$	$7.25^{+0.12}_{-0.12}$	159.02/164
0.57–0.71	$0.704^{+0.014}_{-0.013}$	$1.29^{+0.19}_{-0.18}$	$13.49^{+0.22}_{-0.22}$	$8.57^{+0.14}_{-0.14}$	164.24/178
0.71–0.86	$0.690^{+0.015}_{-0.015}$	$1.21^{+0.19}_{-0.18}$	$10.63^{+0.19}_{-0.19}$	$6.71^{+0.12}_{-0.12}$	168.32/161
0.86–1.00	$0.646^{+0.017}_{-0.017}$	$1.20^{+0.22}_{-0.20}$	$7.56^{+0.16}_{-0.16}$	$4.65^{+0.10}_{-0.10}$	148.12/137

Notes.
[a] N_H is fixed at 4.6×10^{22} cm^{-2} (see F. Coti Zelati et al. 2020) and the cross-calibration constants of the three IXPE DUs are frozen to the values reported in Table 1.
[b] Emission radius extracted from the bbodyrad parameter norm assuming a distance of 4.5 kpc (A. Tiengo et al. 2010).
[c] Total unabsorbed flux in units of 10^{-12} erg cm^{-2} s^{-1}.
[d] Total observed flux in units of 10^{-12} erg cm^{-2} s^{-1}.

Table 3
Energy-dependent PF, and Polarization Degree and Angle

Energy bin	PF (%)	PD (%)	PA (deg)	χ^2/dof
2–3 keV	$31.9^{+1.3}_{-1.3}$	$55.4^{+5.2}_{-5.2}$	$-75.4^{+2.7}_{-2.7}$	97.95/94
3–4 keV	$40.1^{+1.2}_{-1.2}$	$38.3^{+4.9}_{-4.9}$	$-75.7^{+3.7}_{-3.7}$	82.09/94
4–5 keV	$48.7^{+1.1}_{-1.1}$	$58.3^{+8.6}_{-8.6}$	$-78.0^{+4.3}_{-4.3}$	114.52/93
5–6 keV	$56.5^{+1.0}_{-1.0}$	$(40.8^{+19.3}_{-19.3})$	$(-86.2^{+176.2}_{-3.8})$	50.12/46

Note. PF, PD, and PA values are obtained using the XSPEC procedure described in the text, with errors (at 1σ confidence level) derived from the err procedure in XSPEC. Negative PA values are given west of the celestial north. The most-probable values of PD and PA are reported in parenthesis when PD falls below the corresponding MDP_{99}.

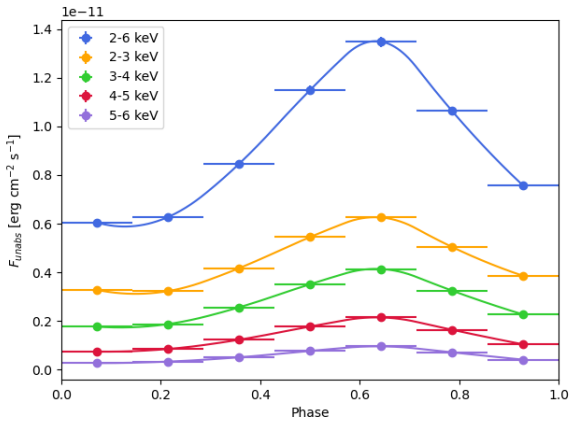

Figure 2. IXPE pulse profile of 1E 1547.0−5408 in the 2–6, 2–3, 3–4, 4–5, and 5–6 keV energy bands; the solid lines are splines connecting the data.

2–3 keV energy bins do not intersect and the former is only tangent to the 4–5 keV one. The polarization angle, instead, is fully consistent with a constant within 1σ confidence level, with an average value of $74\overset{\circ}{.}4 \pm 2\overset{\circ}{.}1$ measured west of north.

3.5. Phase-resolved Polarimetric Analysis

In order to investigate how the polarization properties depend on the rotational phase, we folded the source photon lists into seven equally spaced phase bins as described in Section 3.3, i.e., through the IXPEOBSSIM tools xpphase and xpselect and using the timing solution presented in Section 3.1. We then performed a simultaneous fit of the Stokes spectra within XSPEC using a tbabs×(bbodyrad×polconst) model, with all spectral parameters frozen at those reported in Table 2 in the different phase bins and leaving only the polconstPD and PA as free parameters. The values of the best-fitting parameters are reported in Table 4.

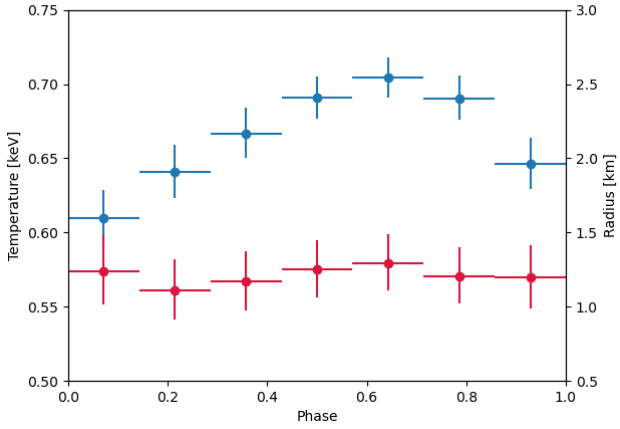

Figure 3. Phase variation of the BB temperature (cyan) and radius (red) for the best-fitting model reported in Table 2.

Figure 6 illustrates the phase-dependent behavior of PD and PA in the range 2–6 keV, with the corresponding pulse profile (see Figure 2) overlayed for comparison. PD is only marginally consistent with a constant (χ^2/dof = 9.38/6, p-value of 0.153), and the most-probable values hint at an anticorrelation with the pulse profile, with the minimum (maximum) of PD occurring in the vicinity of the maximum (minimum) of the pulse profile. In contrast, the polarization angle exhibits a clear oscillation with the rotational phase, around an average value $-74\overset{\circ}{.}3 \pm 1\overset{\circ}{.}5$, consistent (within 1σ) with that derived in Section 3.4 (see Figure 4).

We further analyzed the data by splitting the 2–6 keV range into narrower energy intervals. After exploring different binning schemes, we found that a significant detection (PD > MDP_{99}) is obtained in all phase intervals only in the 2–3 keV and 3–6 keV bands. As shown in Figure 7, the phase-

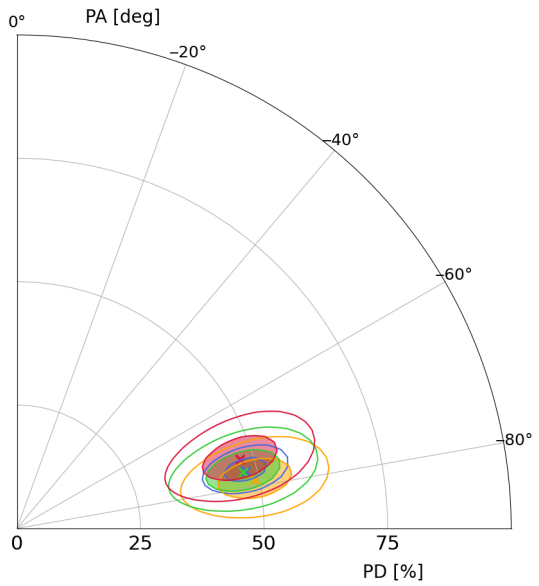

Figure 4. 1E 1547.0−5408 phase- and energy-integrated (2–6 keV) most-probable values for PD and PA (crosses) measured by the three IXPE DUs (DU1 yellow, DU2 green, and DU3 red); the combined result is also shown in blue. Constant PD and constant PA loci are marked by concentric circles and radial lines, respectively, with PA = 0° corresponding to the celestial north and PA decreasing westward. The shaded and empty contours represents the 68% and 99% confidence regions, respectively, obtained using the `steppar` command in XSPEC.

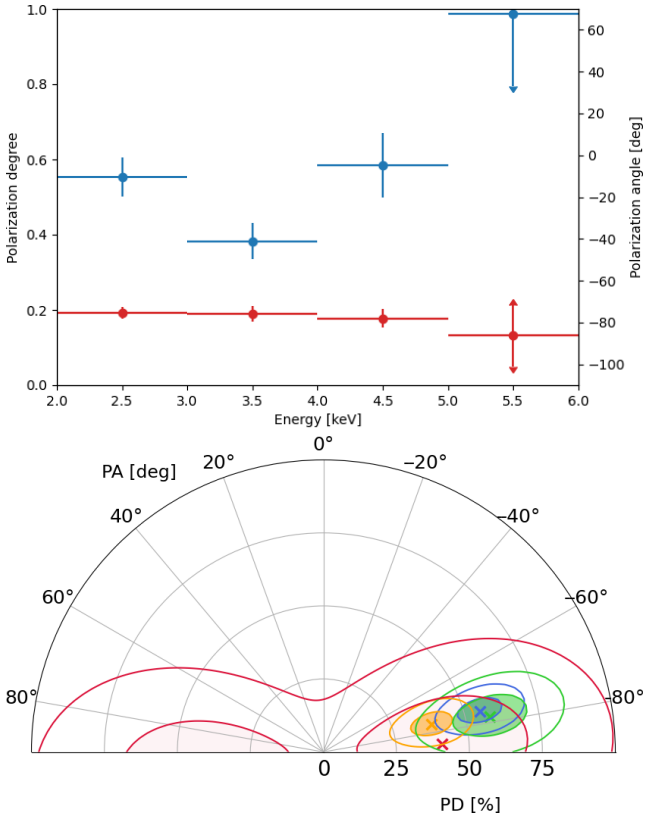

Figure 5. Top: Energy-dependent polarization degree (cyan) and polarization angle (red) obtained with XSPEC (see text for details). Error bars show the 1σ confidence intervals derived with the `err` procedure. When the PD measurement falls below MDP_{99}, a downwards arrow marks the 3σ upper limit; the associated value of PA is unconstrained and is shown by a double-headed arrow. Bottom: Same in the PD-PA plane for the 2–3 (blue), 3–4 (orange), 4–5 (green), and 5–6 keV (red) energy bins; symbols and contour codes are as in Figure 4. All values are reported in Table 3.

dependent polarization degree changes little in the two bands (a difference of more than 1σ appears only in the last phase bin). On the other hand, the polarization angle displays a clear oscillation in both the 2–3 and the 3–6 keV bands, consistent with the behavior in the total energy range.

We fitted the phase-dependent polarization angle with the rotating vector model (RVM; V. Radhakrishnan & D. J. Cooke 1969; M. M. Komesaroff 1970, see H. Tong et al. 2021 and R. Taverna et al. 2022 for a discussion on the RVM model applied to magnetars),

$$\tan(\mathrm{PA} - C) = \frac{\sin\xi \sin[\pm(\gamma + \gamma_0)]}{\sin\chi\cos\xi - \cos\chi\sin\xi\cos(\gamma + \gamma_0)}, \quad (1)$$

where χ and ξ are the angles of the line-of-sight (LOS) and of the magnetic axis with the spin axis, respectively, γ is the rotational phase, γ_0 is an arbitrary initial phase, and C is an angular offset. The plus/minus sign refers to the two possible directions of the star rotation, counterclockwise or clockwise, and reflects the two conventions commonly adopted in the literature about the direction in which the position angle increases in the plane of the sky, clockwise/counterclockwise if a plus/minus sign is placed in front of the fraction in Equation (1), in lieu of the plus/minus sign inside the sine function (J. E. Everett & J. M. Weisberg 2001). For the sake of conciseness, we will refer to the two possible choices for the RVM models as the "plus" (χ_+, ξ_+) and "minus" (χ_-, ξ_-) solutions. It should be noted that, due to the π-periodicity of the arctan function, the configurations ($2\pi - \chi_\pm$, $2\pi - \xi_\pm$), i.e., ($-\chi_\pm$, $-\xi_\pm$), describe equivalent geometries. In order to improve the statistics, we fitted simultaneously the data integrated in the 2–3 and in the 3–6 keV band, treating the two datasets as mutually independent. This is justified on the assumption that the recorded events are Poissonian distributed and the events collected in separate energy channels are physically distinct. Leaving all four parameters in Equation (1) free to vary, the best simultaneous fits yield $\chi_+ = 106.^\circ6 \pm 30.^\circ9$ and $\xi_+ = 157.^\circ7 \pm 4.^\circ0$ for the plus solution and $\chi_- = -73.^\circ4$, $\xi_- = -22.^\circ3$ for the minus one (see Table 5 and Figure 8 for more details). Both pairs of angles provide the same, good fit to the observed PA and, as expected, it is $\xi_- = \xi_+ - \pi$, $\chi_- = \chi_+ - \pi$, which exactly mirrors the two spin orientations. We also verified that the fits of PA integrated throughout the 2–6 keV band yield consistent results within the errors. We corroborated our RVM results with a Bayesian analysis, starting from flat priors in the range $[0, 2\pi]$ for the plus solution, $[-\pi, \pi]$ for the minus solution, $[-2\pi, 2\pi]$ for C and γ_0. The posteriors for the two models are shown in Figure 9; the probability density distributions are clearly the same, much as the best-fitting models in Figure 8, with the only difference of a shift by $-\pi$ in the χ, ξ angles. The best estimates for the parameters derived with both techniques are in close agreement, well within 1σ uncertainties.

Although the RVM fitting provides a well constrained value of the angle ξ between the rotation and the dipole axis, the angle χ between the rotation axis and the LOS is more loosely determined, with an uncertainty of $\sim$30°. Despite these

Table 4
Phase-resolved Polarization Analysis

Phase Bin	PD (%)	PA (deg)	χ^2/dof
2–6 keV			
0.00–0.14	$58.6^{+10.5}_{-10.5}$	$-63.6^{+5.2}_{-5.1}$	228.53/247
0.14–0.29	$76.4^{+9.7}_{-9.7}$	$-79.2^{+3.6}_{-3.6}$	225.15/244
0.29–0.43	$44.0^{+8.2}_{-8.2}$	$86.0^{+5.4}_{-5.4}$	240.34/265
0.43–0.57	$43.1^{+7.0}_{-7.0}$	$88.0^{+4.7}_{-4.7}$	273.30/280
0.57–0.71	$53.5^{+6.4}_{-6.4}$	$-82.3^{+3.4}_{-3.4}$	258.64/294
0.71–0.86	$57.8^{+7.3}_{-7.3}$	$-65.6^{+3.6}_{-3.6}$	276.18/277
0.86–1.00	$65.8^{+9.0}_{-9.0}$	$-48.1^{+3.9}_{-3.9}$	272.99/253
2–3 keV			
0.00–0.14	$65.5^{+17.6}_{-17.6}$	$-66.0^{+7.7}_{-7.9}$	87.99/94
0.14–0.29	$73.1^{+16.7}_{-16.7}$	$-82.4^{+6.4}_{-6.4}$	80.74/91
0.29–0.43	$61.0^{+14.6}_{-14.6}$	$-80.2^{+6.9}_{-6.9}$	83.12/94
0.43–0.57	$42.4^{+12.6}_{-12.6}$	$89.7^{+8.6}_{-8.6}$	85.05/94
0.57–0.71	$61.2^{+11.6}_{-11.6}$	$-78.5^{+5.5}_{-5.5}$	87.49/94
0.71–0.86	$67.5^{+12.9}_{-12.9}$	$-67.7^{+5.5}_{-5.5}$	103.25/94
0.86–1.00	$93.9^{+6.1}_{-15.9}$	$-51.1^{+4.7}_{-4.7}$	88.07/94
3–6 keV			
0.00–0.14	$59.5^{+14.5}_{-14.5}$	$-54.7^{+7.0}_{-7.0}$	129.14/142
0.14–0.29	$78.1^{+13.1}_{-13.1}$	$-77.2^{+4.8}_{-4.8}$	139.02/142
0.29–0.43	$37.7^{+10.8}_{-10.8}$	$89.3^{+8.5}_{-8.5}$	150.40/160
0.43–0.57	$44.9^{+9.3}_{-9.3}$	$85.4^{+6.0}_{-6.0}$	181.47/175
0.57–0.71	$53.4^{+8.4}_{-8.4}$	$-85.7^{+4.5}_{-4.5}$	164.68/189
0.71–0.86	$47.3^{+9.6}_{-9.6}$	$-63.6^{+5.8}_{-5.9}$	157.96/172
0.86–1.00	$59.6^{+12.1}_{-12.1}$	$-47.5^{+5.9}_{-5.9}$	172.56/148

Note. Results are obtained using the XSPEC procedure described in the text. Errors are at 1σ confidence level, derived from the `err` procedure in XSPEC. PA values are given east of the celestial north.

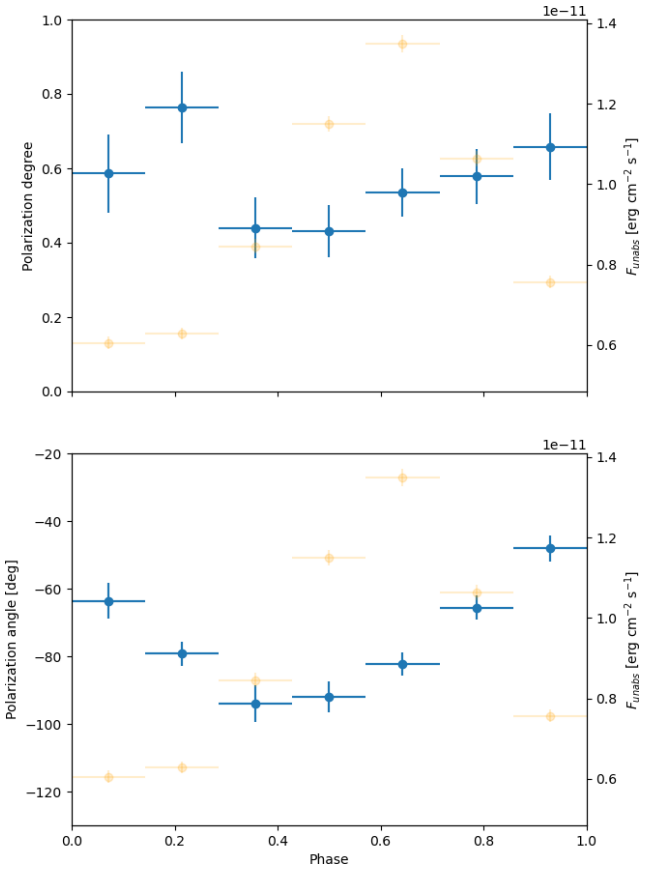

Figure 6. Phase-dependent polarization degree (top) and polarization angle (bottom), integrated over the 2–6 keV range, obtained using XSPEC (cyan, see text for details). Errors are at 1σ, as derived with the XSPEC`err` procedure. Values are reported in Table 4. In both plots, the 2–6 keV pulse profile has been superimposed for ease of comparison (light orange). A shift by $-180°$ was applied to all positive values of PA (third and fourth phase bins, see Table 4) to reproduce a smooth oscillation.

limitations, both solutions point to an inclined rotator seen away from the spin axis. This is at variance with the geometry reported by R. E. Stewart et al. (2025b), $\chi = 5\overset{\circ}{.}2^{+3.2}_{-2.6}$ and $\xi = 2\overset{\circ}{.}4^{+1.4}_{-1.2}$, based on simultaneous Parkes/Murriyang radio data. Our solution for the inclination of the dipole axis, $\xi_+ \sim 158°$, is close to the best estimate, $\xi = 160°$, reported by F. Camilo et al. (2008), using two distinct 2007 Parkes radio observations covering roughly half of the rotational period. However, the value they derived for the inclination of the spin axis, $\chi = 174°$, is different. We also note that a geometry with ($\chi = 174°$, $\xi = 160°$) is inconsistent with the oscillating behavior of PA observed in the radio, since the RVM model with $\chi > \xi$ (χ, $\xi > 90°$) swings from $-90°$ to $90°$. A reanalysis of the same 2007 Parkes data by R. E. Stewart et al. (2025b) suggested a low-obliquity solution, with $\chi = 8\overset{\circ}{.}4^{+5.8}_{-4.2}$ and $\xi = 4\overset{\circ}{.}9^{+3.4}_{-2.4}$.

4. Discussion

Despite the shorter exposure, compared to those of the other magnetars targeted by IXPE (only 1E 1841−045 was observed for a comparable time; M. Rigoselli et al. 2025; R. E. Stewart et al. 2025a), we were able to perform timing, spectral, and polarization analyses of 1E 1547.0−5408, obtaining significant measurements in the 2–6 keV energy band; at higher energies, the background dominates the signal, preventing any meaningful conclusion.

The phase-averaged spectrum turns out to be well described by a single BB component with temperature $\sim$0.7 keV. Folding the data in seven, equally spaced phase intervals, the same spectral model provides a good representation in every phase bin. However, a variation of the temperature with the rotational phase is clearly present, which closely follows the flux modulation, while the emission radius is consistent with being a constant (see Figures 2 and 3). The single-peaked, quasi-sinusoidal pulse shape, the relatively large PF, which increases with energy (see Table 3), and the small BB radius ($\sim$1.2 km) point to a single, fairly small hot spot. The change of $T_{\rm BB}$ along the rotation suggests a complex emission pattern, with radiation coming from a region on the star's surface characterized by a nonuniform temperature distribution, with colder and hotter zones entering in view at different phases.

The large phase- and energy-integrated polarization degree measured by IXPE ($\approx$50%) places 1E 1547.0−5408 alongside the mostly polarized magnetars, 1RXS J1708 (S. Zane et al. 2023) and 1E 1841−045 (M. Rigoselli et al. 2025), the properties of which were interpreted in terms of an atmospheric layer covering the emitting region. The same explanation possibly holds also for 1E 1547.0−5408. In fact, the energy-dependent PD (see Figure 5) reaches values as high as $\approx$60%, which is incompatible with thermal emission from a

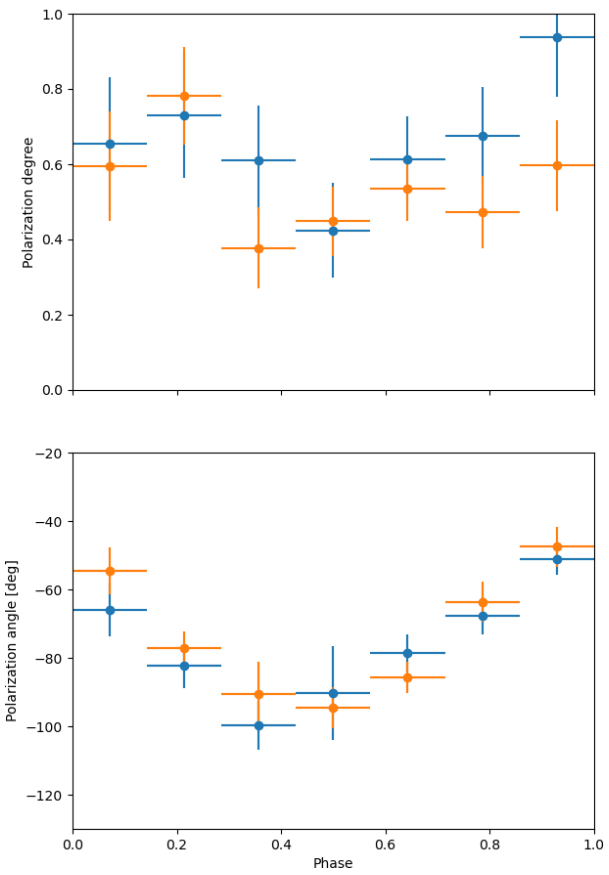

Figure 7. Phase-dependent polarization degree (top) and polarization angle (bottom), integrated over energy in the 2–3 (blue) and 3–6 keV (orange) ranges (errors are at 1σ confidence level; the error bar of PD in the last bin of the top panel is truncated at the maximum attainable value, 1). Details as in Figure 6. Values are reported in Table 4.

bare condensed surface around 2–3 keV and magnetospheric reprocessing via RCS at higher energies (R. Taverna et al. 2020, besides, no evidence for a PL tail was found in the IXPE data).

Although an atmosphere can explain the spectral properties and the large observed PD in 1E 1547.0−5408, the possible presence of a local minimum in the degree of polarization between 3 and 4 keV, if confirmed, poses a challenge because there is no evidence of a second spectral component or prominent spectral features that can explain such behavior.[15] R. E. Stewart et al. (2025b) invoke mode conversion at the vacuum resonance (VR; see G. G. Pavlov & Y. A. Shibanov 1979; A. D. Kaminker et al. 1982; W. C. G. Ho & D. Lai 2003) to explain the decrease in PD, which they estimate to vanish at about 6 keV, with a 90° swing of the polarization angle at the same energy. However, our analysis shows no evidence of either a monotonic decrease with energy or a vanishing polarization at high energies. Indeed, a linear fit to the energy-dependent PD forcing the slope to be negative yields a $\chi^2/\mathrm{dof} = 7.429/2$, and still predicts a PD $\approx 40\%$ at 6 keV, while PA is consistent with being a constant.

Still, the occurrence of mode switching at the VR does not necessarily imply a change in the dominant mode (i.e., a 90° swing in PA). For magnetic fields as high as $\approx 2 \times 10^{14}$ G (the spin-down field of 1E 1547.0−5408, see Section 3.1), mode switching can be partial, meaning that not all *O*-mode photons become X-mode ones (and conversely) at the VR, with the probability of switching between modes depending on the energy of the photon, magnetic field, and density gradient in the atmosphere (W. C. G. Ho & D. Lai 2003). This results in a local minimum in PD, while the polarization angle remains constant with energy (R. M. E. Kelly et al. 2024, 2025, and references therein). To test whether (partial) mode conversion at the vacuum resonance can produce a behavior of PD like that suggested by IXPE between 3 and 4 keV, we performed some simulations following the method detailed in R. M. E. Kelly et al. (2024). Figure 10 shows the energy-dependent behavior of the polarization degree in the case of emission from a single atmospheric patch, assuming a field of strength $B = 2 \times 10^{14}$ G, inclined by $\sim 10°$ with regard to (wrt) the surface normal and a probability threshold of $P_{\rm th} = 0.9$[16] Although a more detailed model is required before any definitive conclusion can be drawn, the results reported in Figure 10 suggest that partial mode conversion at the VR can produce dips in PD at the energies observed by IXPE in 1E 1547.0−5408.

The phase variation of PD is statistically consistent with a constant within 1σ uncertainties. However, the most-probable values hint to an anticorrelation of PD with the pulse profile in the total band (2–6 keV), and also in the 2–3 and 3–6 keV energy intervals (see the top panels of Figures 6 and 7). On the other hand, the polarization angle traces a clean sinusoidal modulation with the rotational phase, which can be well fitted with an RVM (see Figure 8). This pattern is common to other magnetars observed by IXPE and has been interpreted as a signature of vacuum birefringence in the external region close to the star (R. Taverna et al. 2022; S. Zane et al. 2023; J. Heyl et al. 2024). While PD bears the imprint of the (complex) thermal and magnetic maps on the star's surface, much as the pulse profile, PA is determined at larger distances where the topology of the field is largely dipolar. This is a consequence of vacuum birefringence, which forces the polarization vectors to follow the magnetic field direction up to the polarization-limiting radius ($r_{\rm pl} \approx 100\, R_{\rm NS}$ for magnetars; J. S. Heyl et al. 2003; R. Taverna et al. 2015).

According to R. E. Stewart et al. (2025b), who fitted the polarization angle measured in the radio band with the Parkes/Murriyang telescope, the star is an almost aligned rotator, seen nearly along the magnetic axis. In this case, for photons coming from regions very close to the pole, the polarization vectors at emission would corotate with the star, following the magnetic field near the pole. As a consequence, if vacuum birefringence is neglected, the phase-averaged polarization degree observed at infinity should be significantly lower than what is expected when a proper account for QED effects is made, even assuming that emitted photons are polarized mostly in one mode. This is one of the points that led R. E. Stewart et al. (2025b) to claim that the high phase-

[15] Especially for small emitting spots, propagation across the quasi-tangential (QT) region, where the photon propagation direction is nearly parallel to the magnetic field lines, can reduce the observed PD. However, the depolarization occurs at energies well below the IXPE band for magnetic fields $\gtrsim 10^{14}$ G (C. Wang & D. Lai 2009).

[16] The magnetic field used in the simulation of Figure 10 is somewhat smaller than the polar value inferred in 1E 1547.0−5408 because convergence issues with our atmospheric code prevented us from reaching higher values of *B*. We successfully produced a run with an aligned field of $B = 4 \times 10^{14}$ G on a coarser energy grid, which, albeit noisier, is consistent with the results shown in Figure 10.

Table 5
RVM Fit of the Polarization Angle

	χ (deg)	ξ (deg)	C (deg)	γ_0 (deg)	χ^2/dof
Plus solution	106.60 ± 30.85	157.73 ± 4.04	−75.35 ± 1.62	−69.93 ± 5.15	5.227/10
Minus solution	−73.40 ± 30.85	−22.27 ± 4.04	−75.35 ± 1.62	−69.93 ± 5.15	5.227/10

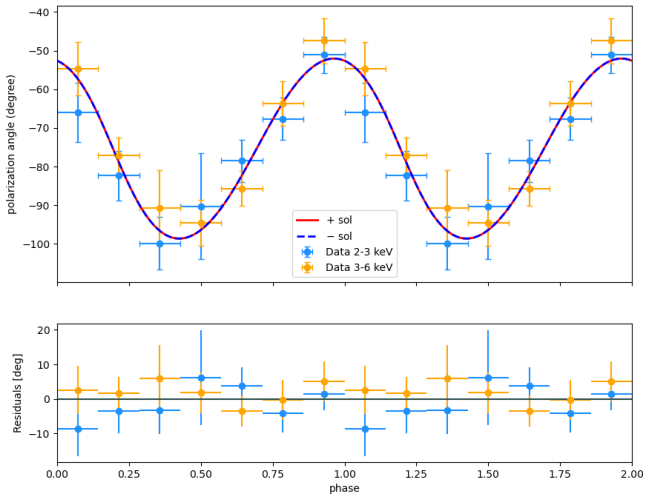

Figure 8. IXPE 2–3 keV (cyan) and 3–6 keV (orange) polarization angle simultaneously fitted by an RVM (see Table 5); two rotational cycles are shown for ease of visualization. The red solid (blue dotted) line shows the best-fitting plus (minus) solution; residuals are shown in the bottom panel.

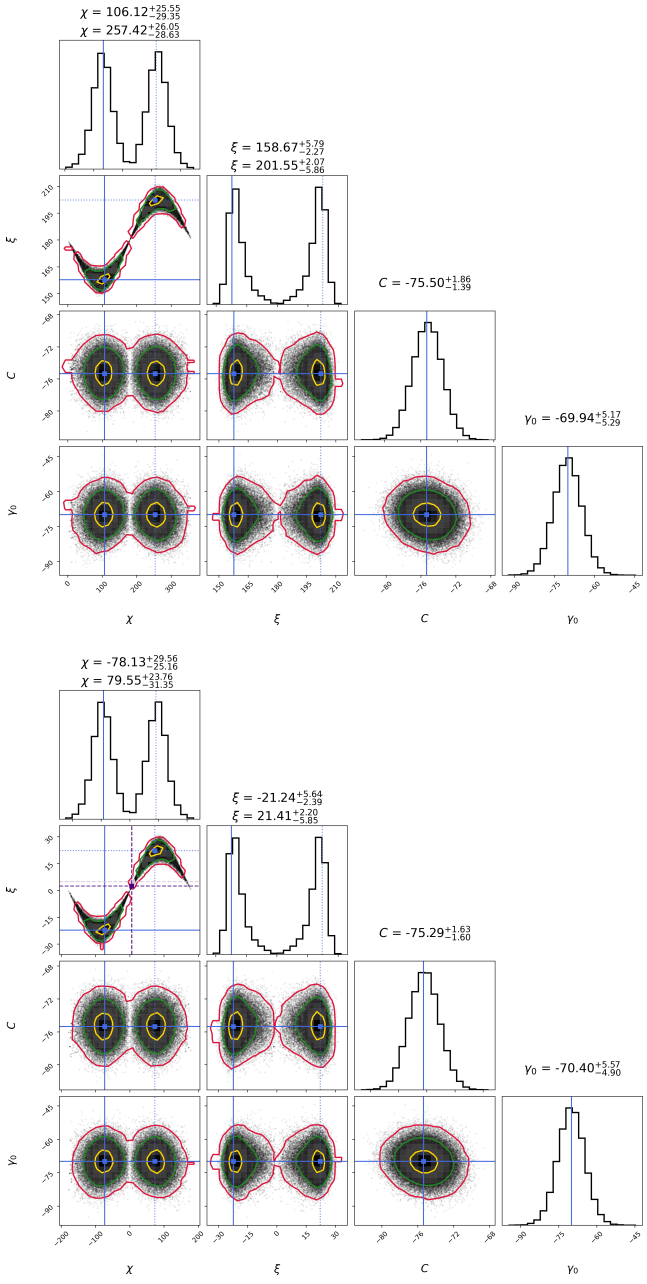

Figure 9. Marginalized posterior distributions for the RVM plus (top) and minus (bottom) solutions. The best-fit values ($\chi_\pm$, $\xi_\pm$), obtained through χ^2 minimization, as well as the mirrored solutions ($2\pi - \chi_\pm$, $2\pi - \xi_\pm$) are marked by solid and dotted blue lines, respectively. The 1, 2, and 3σ confidence contours are shown in yellow, green, and red, respectively. The maximum a posteriori estimates, along with their associated 1σ uncertainties, are reported above each 1D histogram. The best-fit values from the radio analysis by R. E. Stewart et al. (2025b), $\chi = 5.^\circ2$, $\xi = 2.^\circ4$ (dashed violet lines) and $\chi = 8.^\circ4$, $\xi = 4.^\circ9$ (dashed pink lines), are also shown for comparison.

averaged and phase-resolved polarization degree detected by IXPE in 1E 1547.0−5408 is a compelling test of vacuum birefringence.

Our RVM fit of PA measured by IXPE produces a different geometry, with a net inclination between the magnetic and rotation axes of ∼20° and the LOS tilted by ∼75° wrt the rotation axis. The nearly aligned geometries proposed by R. E. Stewart et al. (2025b) are, according to our posteriors, excluded with significance $\gtrsim$90%.

In the geometry we found, the difference in the degree of polarization obtained with or without accounting for vacuum birefringence is expected to be negligible because of the limited extent of the emission region and of the strong magnetic field of the source. In such cases, in fact, the change in the magnetic field direction across the emitting area is quite small, mimicking the conditions that would generally occur at a large distance from the source ($r_{\rm pl} \approx 100 R_{\rm NS}$, C. Wang & D. Lai 2009).

To provide a quantitative estimate, we performed a simulation using the ray-tracing code discussed in R. Taverna et al. (2015). General relativistic corrections, both in the photon trajectories and in the magnetic field, are accounted for. We assumed a neutron star mass and radius of $M = 1.4\,M_\odot$ and $R = 12$ km, respectively, and a (polar) value of the dipole field $B \sim 5 \times 10^{14}$ G. The emission comes from a circular spot centered on the magnetic pole with semiaperture $\theta \approx 6^\circ$, corresponding to $R_{\rm BB} \approx 1.2$ km (as evaluated by a distant observer, see Table 1). The spot is divided into a hot ($kT_{\rm h} = 0.87$ keV, $\theta_{\rm h} \approx 3^\circ$) cap with a large intrinsic polarization (80%), surrounded by a warm ($kT_{\rm w} = 0.76$ keV)

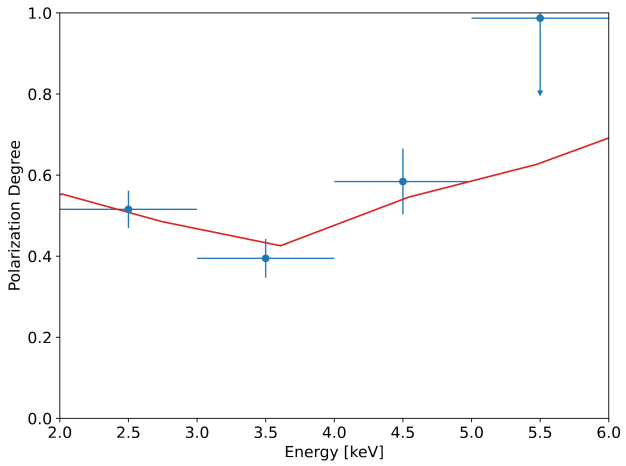

Figure 10. Energy-dependent polarization degree (red) at the surface of an atmospheric patch including partial mode conversion at the VR. Here, the inclination of the magnetic field to the surface normal is $\sim 10^{\circ}$ and the field strength 2×10^{14} G. The observed polarization degree is also shown (cyan) to facilitate visual comparison.

annulus, extending from 3° to 6°, with a lower polarization (30%); the rest of the surface is cold, at $kT_{\rm c} = 0.15$ keV. Both regions emit isotropic BB radiation and the (constant) polarization degrees were chosen in such a way to recover the observed PD in the IXPE band. All previous quantities are measured by a stationary observer at the star's surface, unless explicitly stated otherwise.

The results, shown in Figure 11 for our geometry, are qualitatively in agreement with the IXPE measurements in the 2–6 keV band, and successfully reproduce the single-peaked pulse profile, a nearly constant phase-dependent polarization degree (weakly anticorrelated with the light curve), and a clear sinusoidal oscillation of the polarization angle. Actually, emission from a more realistic magnetized atmosphere model is not expected to be isotropic. In order to test if and to which extent magnetic beaming can influence the results presented in Figure 11, we computed some models replacing the Planck function, B_{ν}, with $B_{\nu} f(\mu)$, where $\mu = \cos\theta_{\rm Bk}$ is the cosine of the angle between the local magnetic field and the ray. The beaming factor $f(\mu)$ was taken to qualitatively reproduce the angular pattern of the intensity emerging from a strongly magnetized atmosphere (e.g., F. Özel 2001). However, only small deviations in the pulse profiles were found: fractional differences in the PF are typically $\lesssim$10%) while both PD and PA are pretty much unchanged. At any rate, and as for the model shown in Figure 10, we stress that this simple model is not intended to faithfully match all the observed features, but rather to demonstrate that the derived viewing geometry and emission configuration produce results consistent with the observations. As expected, the polarization degree calculated with or without considering vacuum birefringence (solid and dashed lines in the central panel) is nearly indistinguishable, so no compelling argument about the presence of vacuum birefringence can be made.

In this respect, it is worth drawing some comparisons between our analysis and that of the magnetar 1RXS J1708 presented in S. Zane et al. (2023). Here, we have shown that a simple emission model, which relies on the source geometry inferred from the RVM fit of the IXPE polarization angle, can broadly reproduce the main X-ray properties of the source. In

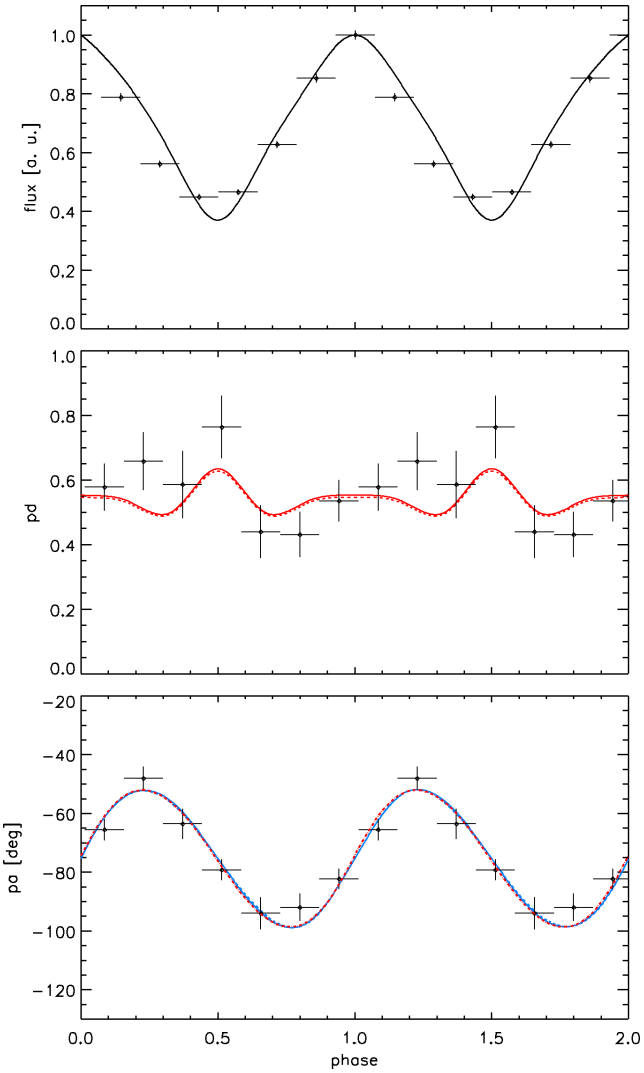

Figure 11. Pulse profile (normalized to the maximum, top), phase-dependent PD (middle), and PA (bottom) as obtained from the ray-tracing code discussed in R. Taverna et al. (2015), using χ_{-} and ξ_{-} (red dashed–dotted line in the bottom panel). The emitting region is a circular spot at the magnetic pole (see text for details). Solid and dashed lines show the results obtained with and without including vacuum birefringence effects, respectively. IXPE data are also shown (black points with error bars). Both flux and PD/PA points have been phase-shifted back by ≈0.65 cycles wrt Figures 2, 6, and 7 to facilitate visual comparison.

the case of 1RXS J1708, a somewhat reverse approach was followed. First, possible emission geometries capable of explaining the (energy-dependent) spectropolarimetric data were explored, and then these were contrasted with the phase variation of PA and with the RVM best fit. The agreement they found is only qualitative, not surprisingly given that no real fit of PA with their models was attempted.

The relatively large half-opening angle of the radio beam required by our X-ray-favored geometry to match the observed duty cycle ($\rho \sim 22^{\circ}$) does not necessarily invalidate the model. Although the empirical relation $\rho \sim 5^{\circ}/\sqrt{P}$ predicts a much narrower beam ($\sim 3\overset{\circ}{.}4$ for a period 2.1 s), this scaling is derived primarily from ordinary rotation-powered pulsars. 1E 1547.0 −5408 is a high-energy magnetar with a rotational loss rate ($\dot{E} \sim 9 \times 10^{34}$ erg s^{-1}) and magnetic field strength far exceeding the population used to establish such relations. Given the significant scatter in beam widths observed

even among ordinary pulsars (see e.g., S. Johnston & A. Karastergiou 2019), and the unique magnetospheric physics of magnetars, an opening angle $\rho \sim 22^{\circ}$ cannot be ruled out.

5. Conclusions

In this work, we presented an analysis of the 500 ks IXPE observation of the AXP 1E 1547.0−5408. We found that the source X-ray emission is essentially thermal, with only one BB component contributing at each phase of the star's rotation and comes from a fairly limited region on the star's surface ($R_{\rm BB} \approx 1.2$ km) with nonuniform properties, as suggested by the modulation of the temperature with phase.

Both the relatively high phase-averaged and phase-resolved polarization degrees are consistent with emission from a magnetized atmospheric layer covering (part of) the star surface. The constancy of the polarization angle with energy implies that radiation is polarized in the same mode throughout the IXPE band, as predicted for an ultramagnetized atmosphere, the emission of which is expected to be X-mode dominated (R. M. E. Kelly et al. 2024). The only potential evidence of QED effects in the atmospheric medium (vacuum +plasma) comes from the dip in the degree of polarization that is possibly present around 3–4 keV, which may indeed be a signature of partial mode conversion at the vacuum resonance.

On the other hand, the RVM provides a very good interpretation of the modulation in phase of the polarization angle measured by IXPE and this hints at the presence of vacuum birefringence in the star's magnetosphere (R. Taverna et al. 2022). In the geometry we inferred from the RVM fit, 1E 1547.0−5408 is an inclined rotator seen nearly perpendicular to the spin axis and this is consistent with the observed pulse profile, assuming isotropic thermal emission from a polar hot spot on the star's surface. The geometry derived by R. E. Stewart et al. (2025b) from radio data points to an almost aligned rotator seen close to the pole, which is unlikely on the basis of IXPE data alone. Still, given that it falls at the boundary of our 3σ contour (see Figure 9), it cannot be excluded, potentially removing the tension between the measures in the two bands. On the other hand, since the RVM constrains the source geometry independently of the assumed emission model, the magnetic field topology in the regions responsible for the radio and the X-ray emission may be different. Further multiwavelength observations of 1E 1547.0−5408 are needed to clarify this issue.

The actual source geometry has an impact on the conclusions one can draw about the presence of QED effects. In the case of an inclined geometry, such as the one derived here, the polarization degree of radiation emitted from a small spot is maintained up to the observer for magnetar-like fields, and no claim about the presence of vacuum birefringence can be made, no matter how large the polarization degree is. In this respect, 1E 1547.0−5408 is no different from other persistent magnetars observed in polarized X-rays (e.g., 1RXS J1708 and 1E 1841−045), confirming that such sources are not ideal targets for (indirect) tests of QED, unless the emission comes from a reasonably extended portion of the surface.

A significant step forward is expected from observations of transient magnetars in outburst, during which emission is indeed expected to emerge from wide hot spots. Another promising class of sources is that of X-ray dim isolated neutron stars (XDINSs), which are also strongly magnetized (albeit with fields typically an order of magnitude lower than those of magnetars, see R. Turolla 2009), the prototypical and brightest member of which, RX J1856.5−3754, exhibits a very low X-ray PF (N. Sartore et al. 2012), making them key targets for testing vacuum birefringence with future instruments capable of probing polarization at sub-keV energies (see e.g., R. M. E. Kelly et al. 2025, for predictions in the soft X-rays and R. P. Mignani et al. 2017 for a potential QED detection in the optical). Next-generation X-ray polarimeters, such as the Enhanced X-ray Timing and Polarimetry mission (eXTP, S.-N. Zhang et al. 2025) and the Enhanced X-ray Polarimetry Observatory (EXPO, recently proposed for the ESA medium-size mission call), with their superior sensitivity and fast-repointing capabilities in the medium-to-high-energy X-ray band, and the Globe Orbiting Soft X-ray polarimeter concept (GOSoX, H. L. Marshall et al. 2021), which will observe in the soft-X band, will hopefully provide the definitive answer on the long-sought-after test of vacuum birefringence, finally bridging the gap between fundamental physics and astrophysical observations of neutron stars.

Acknowledgments

We gratefully acknowledge the anonymous referee for their constructive criticism and helpful remarks. This research was supported by the International Space Science Institute (ISSI) in Bern, through the International Team project 25-657 "Polarimetric Insights into Extreme Magnetism". The work of R. Ta., R. Tu., and L. M. is partially funded by the PRIN 2022—project 2022LWPEXW—"An X-ray view of compact objects in polarized light," European Union funding—Next Generation EU, Mission 4 Component 1, CUP C53D23001180006. R. M.E.K. is supported by The Science and Technology Facilities Council (STFC) via a PhD studentship (grant No. ST/W507891/1). G.L.I. and S.M. acknowledge financial support from INAF through the Bando Ricerca Fondamentale INAF 2024, Large Grant "TULiP" and GO Grant "Toward Neutron Stars Unification," respectively. A.B. acknowledges support through the European Space Agency (ESA) research fellowship program.

ORCID iDs

Roberto Taverna https://orcid.org/0000-0002-1768-618X
Roberto Turolla https://orcid.org/0000-0003-3977-8760
Lorenzo Marra https://orcid.org/0009-0001-4644-194X
Ruth M.E. Kelly https://orcid.org/0000-0002-5004-3573
Alice Borghese https://orcid.org/0000-0001-8785-5922
Gian Luca Israel https://orcid.org/0000-0001-5480-6438
Sandro Mereghetti https://orcid.org/0000-0003-3259-7801
Andrea Possenti https://orcid.org/0000-0001-5902-3731
Silvia Zane https://orcid.org/0000-0001-5326-880X
Michela Rigoselli https://orcid.org/0000-0001-6641-5450

References

Arnaud, K. A. 1996, ASPC, 101, 17
Bachetti, M. 2018, HENDRICS: High ENergy Data Reduction Interface from the Command Shell, Astrophysics Source Code Library, ascl:1805.019
Bachetti, M., Harrison, F. A., Cook, R., et al. 2015, ApJ, 800, 109
Baldini, L., Bucciantini, N., Lalla, N. D., et al. 2022, ixpeobssim: Imaging X-ray Polarimetry Explorer Simulator and Analyzer, Astrophysics Source Code Library, ascl:2210.020
Bernardini, F., Israel, G. L., Stella, L., et al. 2011, A&A, 529, A19
Camilo, F., Reynolds, J., Johnston, S., Halpern, J. P., & Ransom, S. M. 2008, ApJ, 679, 681

Chen, C.-T. & IXPE Science Operation Center 2025, AAS Meeting, 245, 260.01
Coti Zelati, F., Borghese, A., Rea, N., et al. 2020, A&A, 633, A31
Coti Zelati, F., Rea, N., Pons, J. A., Campana, S., & Esposito, P. 2018, MNRAS, 474, 961
De Grandis, D., Turolla, R., Taverna, R., et al. 2022, ApJ, 936, 99
Di Marco, A., Soffitta, P., Costa, E., et al. 2023, AJ, 165, 143
Duncan, R. C., & Thompson, C. 1992, ApJL, 392, L9
Everett, J. E., & Weisberg, J. M. 2001, ApJ, 553, 341
Fernández, R., & Davis, S. W. 2011, ApJ, 730, 131
Fernández, R., & Thompson, C. 2007, ApJ, 660, 615
Gnedin, Y. N., Pavlov, G. G., & Shibanov, Y. A. 1978a, JETPL, 27, 305
Gnedin, Y. N., Pavlov, G. G., & Shibanov, Y. A. 1978b, SvAL, 4, 117
Harding, A. K., & Lai, D. 2006, RPPh, 69, 2631
Heyl, J., Taverna, R., Turolla, R., et al. 2024, MNRAS, 527, 12219
Heyl, J. S., & Hernquist, L. 1997, JPhA, 30, 6485
Heyl, J. S., Shaviv, N. J., & Lloyd, D. 2003, MNRAS, 342, 134
Ho, W. C. G., & Lai, D. 2003, MNRAS, 338, 233
Johnston, S., & Karastergiou, A. 2019, MNRAS, 485, 640
Kaminker, A. D., Pavlov, G. G., & Shibanov, I. A. 1982, Ap&SS, 86, 249
Kaspi, V. M., & Beloborodov, A. M. 2017, ARA&A, 55, 261
Kelly, R. M. E., Marshall, H. L., Zane, S., et al. 2025, ApJ, 987, 113
Kelly, R. M. E., Zane, S., Turolla, R., & Taverna, R. 2024, MNRAS, 528, 3927
Komesaroff, M. M. 1970, Natur, 225, 612
Lai, D. 2023, PNAS, 120, e2216534120
Lower, M. E., Younes, G., Scholz, P., et al. 2023, ApJ, 945, 153
Luo, J., Ransom, S., Demorest, P., et al. 2021, ApJ, 911, 45
Manchester, R. N., Hobbs, G. B., Teoh, A., & Hobbs, M. 2005, AJ, 129, 1993
Marshall, H. L., Heine, S. N. T., Garner, A., et al. 2021, SPIE, 11444, 114442Y
Mignani, R. P., Testa, V., González Caniulef, D., et al. 2017, MNRAS, 465, 492
Nobili, L., Turolla, R., & Zane, S. 2008, MNRAS, 386, 1527
Özel, F. 2001, ApJ, 563, 276
Pavlov, G. G., & Shibanov, Y. A. 1979, JETP, 49, 741
Piconcelli, E., Jimenez-Bailón, E., Guainazzi, M., et al. 2004, MNRAS, 351, 161
Radhakrishnan, V., & Cooke, D. J. 1969, ApL, 3, 225
Rigoselli, M., Taverna, R., Mereghetti, S., et al. 2025, ApJL, 985, L34
Sartore, N., Tiengo, A., Mereghetti, S., et al. 2012, A&A, 541, A66
Stewart, R. E., Dinh Thi, H., Younes, G., et al. 2025b, arXiv:2509.19446
Stewart, R. E., Younes, G. A., Harding, A. K., et al. 2025a, ApJL, 985, L35
Strohmayer, T. E. 2017, ApJ, 838, 72
Taverna, R., Muleri, F., Turolla, R., et al. 2014, MNRAS, 438, 1686
Taverna, R., & Turolla, R. 2024, Galax, 12, 6
Taverna, R., Turolla, R., Gonzalez Caniulef, D., et al. 2015, MNRAS, 454, 3254
Taverna, R., Turolla, R., Muleri, F., et al. 2022, Sci, 378, 646
Taverna, R., Turolla, R., Suleimanov, V., Potekhin, A. Y., & Zane, S. 2020, MNRAS, 492, 5057
Thompson, C., & Duncan, R. C. 1993, ApJ, 408, 194
Thompson, C., Lyutikov, M., & Kulkarni, S. R. 2002, ApJ, 574, 332
Tiengo, A., Vianello, G., Esposito, P., et al. 2010, ApJ, 710, 227
Tong, H., Wang, P. F., Wang, H. G., & Yan, Z. 2021, MNRAS, 502, 1549
Turolla, R. 2009, ASSL, 357, 141
Turolla, R., Taverna, R., Israel, G. L., et al. 2023, ApJ, 954, 88
Turolla, R., Zane, S., & Watts, A. L. 2015, RPPh, 78, 116901
Verner, D. A., Ferland, G. J., Korista, K. T., & Yakovlev, D. G. 1996, ApJ, 465, 487
Wang, C., & Lai, D. 2009, MNRAS, 398, 515
Weisskopf, M. C., Guainazzi, M., Jahoda, K., et al. 2010, ApJ, 713, 912
Weisskopf, M. C., Soffitta, P., Baldini, L., et al. 2022, JATIS, 8, 026002
Wilms, J., Allen, A., & McCray, R. 2000, ApJ, 542, 914
Zane, S., Taverna, R., González-Caniulef, D., et al. 2023, ApJL, 944, L27
Zhang, S.-N., Santangelo, A., Xu, Y., et al. 2025, SCPMA, 68, 119502